UAB
Universitat Autònoma de Barcelona

Dipòsit digital de documents de la UAB

This is the **submitted version** of the journal article:

Montaña-Mora, Guillem [et al.]. «Oxophilic Sn to Promote Glucose Oxidation to Formic Acid in Ni Nanoparticles». *ChemSusChem*, Vol. 18, Num. 4 (February 2025), art. e202401256 DOI 10.1002/cssc.202401256

This version is available at https://ddd.uab.cat/record/326339

under the terms of the IN COPYRIGHT license.

Oxophilic Sn to promote glucose oxidation to formic acid in Ni nanoparticles

Guillem Montaña-Mora[a,b], Karol V. Mejia-Centeno[a,c], Xueqiang Qi[d], Qian Xue[d], Jesus Chacón-Borrero[a], Francesco Salutari[e], Maria Chiara Spadaro[e,f], Teresa Andreu[c], Germán Salazar-Alvarez[g], Frank Güell[b], Jordi Llorca[h], Jordi Arbiol[e,i], Paulina R. Martinez-Alanis[a], and Andreu Cabot[a,i].

a. Catalonia Institute for Energy Research–IREC, Jardins de les Dones de Negre 1, 2ª pl., Sant Adrià de Besòs, Spain

b. Facultat de Física, Universitat de Barcelona, Carrer de Martí i Franquès, Barcelona 08028, Spain.

c. Facultat de Química, Universitat de Barcelona, Carrer de Martí i Franquès, Barcelona 08028, Spain.

d. School of Chemistry and Chemical Engineering, Chongqing University of Technology, Chongqing 400054, China.

e. Catalan Institute of Nanoscience and Nanotechnology (ICN2), CSIC and BIST, Campus UAB, Bellaterra, 08193 Barcelona, Catalonia, Spain.

f. Department of Physics and Astronomy 'Ettore Majorana', University of Catania, and CNR-IMM, Via S. Sofia 64, 95123 Catania, Italy.

g. Department of Materials Science and Engineering, Ångström Laboratory, Uppsala University, 751 03 Uppsala, Sweden.

h. Institute of Energy Technologies, Department of Chemical Engineering and Barcelona Research Center in Multiscale Science and Engineering, Universitat Politècnica de Catalunya, EEBE, Eduard Maristany 10-14, 08019 Barcelona, Spain.

i. ICREA Pg. Lluis Companys, 08010 Barcelona, Catalonia, Spain.

Abstract

The electrochemical glucose oxidation reaction (GOR) presents an opportunity to produce hydrogen and high-value chemical products. Herein, we investigate the effect of Sn in Ni nanoparticles for the GOR to formic acid (FA). Electrochemical results show that the maximum activity is related to the amount of Ni, as Ni sites are responsible for catalyzing the GOR via the $NiOOH/Ni(OH)_2$ pair. However, the GOR kinetics increases with the amount of Sn, associated with an enhancement of the OH^- supply to the catalyst surface for $Ni(OH)_2$ reoxidation to NiOOH. NiSn nanoparticles supported on carbon nanotubes (NiSn/CNT) exhibit excellent current densities and direct GOR via C-C cleavage mechanism, obtaining FA with a Faradaic efficiency (FE) of 93% at 1.45 V vs. reversible hydrogen electrode. GOR selectivity is further studied by varying the applied potential, glucose concentration, reaction time, and temperature. FE toward FA production decreases due to formic overoxidation to carbonates at low glucose concentrations and high applied potentials, while acetic and lactic acids are obtained with high selectivity at high glucose concentrations and 55 °C. Density functional theory calculations show that the SnO_2 facilitates the adsorption of glucose on the surface of Ni and promotes the formation of the catalytic active Ni^{3+} species.

Keywords: Glucose oxidation reaction, nickel oxohydroxide, formic acid, electrochemical oxidation, hydrogen

Introduction

Glucose is one of the main biomass-derived compounds in terms of production volume, cost, safety, potential uses, and ease of transportation and storage. While primarily used in the food industry, it finds additional applications in the production of bioplastics and biofuels as well as in pharmaceutical and cosmetic manufacturing. Besides, the electrooxidation of glucose (GOR) can be also coupled with the hydrogen evolution reaction (HER) for energy-efficient hydrogen production. As an alternative to the oxygen evolution reaction (OER, 1.23 V vs RHE), the GOR offers a much lower oxidation potential (0.05 V vs RHE). Additionally, within this coupled system, the GOR can be used to produce several value-added chemical compounds and fuels under mild synthesis conditions. Among others, the value-added glucose oxidation products range from 6C species such as gluconic acid and glucaric acid (GRA) down to oxalic acid (OXA) and formic acid (FA). The relatively large number of carbons in the structure increases the complexity of the reaction mechanisms in action and the related challenge of maximizing product selectivity. Two main mechanisms with a complex interconnection have been proposed in the literature (Scheme 1). A first GOR pathway consists of the sequential oxidation of the aldehyde and alcohol functional groups located at the edges of the molecule generating gluconic acid followed by glucuronic acid, and eventually GRA.[1] A second GOR mechanism involves the cleavage of one of the C-C bonds. This cleavage predominantly occurs at the glucose edge, shortening it by one carbon atom at each step, to enter the glyceraldehyde/dihydroxyacetone route to finally yield lactic acid (LA, 3-C), OXA (2-C) and FA (1-C).[2–4] The 5C, 4C, and 3C compounds can be generally produced with lower selectivity due to the difficulty in precisely stopping the C-C cleavage reaction at early stages. Glucose can additionally isomerize to fructose under basic conditions and also enter the glyceraldehyde/dihydroxyacetone route.[5] Glyceraldehyde/dihydroxyacetone further oxidizes to form either glyceric acid or LA, respectively, that further oxidizes to tartronic acid (TA) or acetic acid (AA) and FA, respectively.[3],[6]

Among the possible GOR products, the selective production of FA is particularly interesting owing to its extensive use in various sectors such as agriculture, water treatment, medicines, and especially in the food, chemical, and textile industries. Besides, in the energy field, the development of direct FA/formate fuel cells (DFAFC/DFFC) is a topic of major interest due to their high potential energy density, safe fuel transportation and storage, and superior theoretical cell potential.[7–9] In addition, the oxidation of each glucose molecule all the way down to FA provides 10 e^- that can be used to produce 5 H_2 molecules.

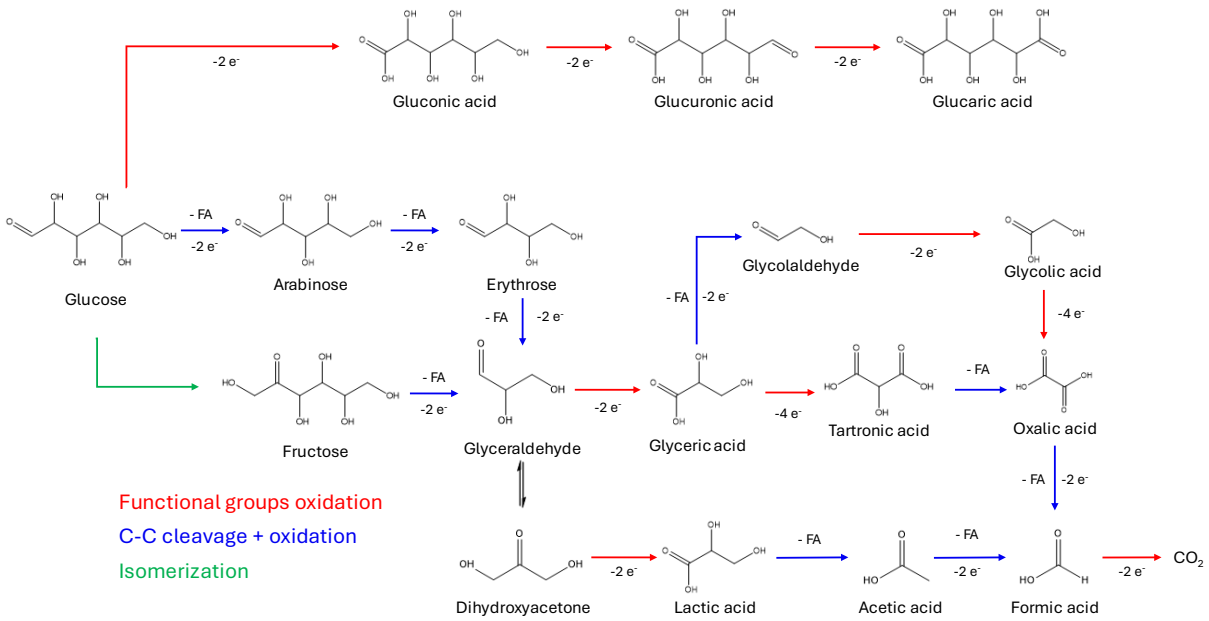

Scheme 1. Scheme of some of the possible GOR pathways.

The multiple GOR pathways and products underscore the importance of developing highly active but at the same time selective electrocatalysts. While noble metals such as Pt, Au, or Rh are commonly used for the electrooxidation of biomass-derived products, their scarcity and high price limit their industrial application. Among the alternative catalytic materials, Ni-based compounds are particularly attractive electrocatalysts in basic media due to their impressive activity, high abundance, low cost, and reduced toxicity. In an alkaline media cell, the GOR mechanism generally relies on the conversion of the surface of the Ni-based material to $Ni(OH)_2$. Then, under GOR operation conditions, when injecting electrons at the cathode and withdrawing them from the anode at a proper potential, the Ni(II) ions at the anode are further oxidized to Ni(III), in the form of nickel oxyhydroxide (NiOOH). The formation of this NiOOH triggers the GOR, thus Ni(III) is considered the catalytic active species. In the process of biomass electrooxidation, Ni(III) acts as an electron acceptor, receiving an electron from the glucose molecule, thus reducing back to Ni(II). Subsequently, the electrode re-oxidizes this Ni(II) to Ni(III) by withdrawing another electron, completing the cycle. This cyclic electron transfer, involving the reduction and subsequent re-oxidation of nickel ions, plays a pivotal role in the GOR mechanism and depends on the ability to exchange electrons with the electrode, the availability of OH^- groups on the catalyst surface, and the adsorption of the glucose and intermediate molecules: [10]

$$Ni + 2OH^- \rightarrow Ni(OH)_2 + 2e^- \quad (1)$$

$$Ni(OH)_2 + OH^- \rightarrow H_2O + NiOOH + e^- \quad (2)$$

$$Glucose + NiOOH \rightarrow Product + Ni(OH)_2 \quad (3)$$

While nickel is widely acknowledged for its outstanding catalytic activity and versatility in facilitating a broad range of reactions, it is also commonly noted for its lack of selectivity and stability.[4,11–14] Thus, several strategies have been developed to overcome these issues. One main approach is the formation of Ni alloys to adjust the surface electronic structure and introduce additional anchoring and catalytic sites. In this direction, Ni has been combined with several other transition metals such as Fe and Co within oxides, nitrides, and chalcogenides, among others.[1,15–17] Yu et al. reported $NiFeO_x$ and $NiFeN_x$ compounds that convert glucose via the functional groups oxidation mechanism, achieving a maximum Faradaic efficiency (FE) of 87% for GNA plus GRA.[1] Lin et al. synthesized $NiCoSe_x$ as a bifunctional catalyst for both GOR and HER, that directs the reaction through the C-C bond cleavage pathway, achieving a FE for formate of 70%.[17] Moreover, Wei et al. catalyzed the GOR mainly to FA with a FE of 86 % using a Mn-doped nickel iron phosphate.[18]

Alternatively, alloying noble metals such as Pd and Pt with p-block elements such as Sn, with higher oxophilicity, has been demonstrated as an excellent strategy to promote electrooxidation.[19] As an example, Brouzgou et al. reported that Pd_3Sn_2/C and PdSn/C exhibited higher electrocatalytic activity and stability than Pd/C towards the GOR.[20] Our group and others have also demonstrated the high activity and enhanced stability of PdSn and PtSn-based catalysts towards ethanol and formate oxidation.[21–24] The presence of Sn within the alloy or SnO_2 forming a composite has two important effects. On the one hand, Sn can alter the interaction with reactants/products, stabilizing intermediates. This adjustment of adsorption energies between reactants and catalyst surface sites can significantly alter, and potentially even entirely redirect, the reaction pathway.[25] In this direction, Tang et al. showed how within a Pt-Sn catalyst the charge transfer from Sn to Pt facilitates the C-O and C-C polarization, thus promoting complete ethanol oxidation to CO_2.[26] On the other hand, the oxophilic character of Sn and readily formation of $Sn(OH)_x$ species contributes to promoting water activation at low potentials, providing oxygen-containing species (OH_{ads}) to the surface. In this way, Sn promotes oxidation reactions by lowering the oxidation barriers through hydrogen-bond interactions.[27] As an example in this direction, Du et al. showed that the addition of Sn to Pd promoted AA production through the ethanol oxidation reaction.[24] Besides, Liu et al. demonstrated that Pt-SnO_2 core-shell heterostructures facilitate C-C cleavage by the oxidation of CO_{ads} and $CH_{x,ads}$ promoted in the presence of OH_{ads} formed at Sn sites.[28] In the particular case of Ni, the presence of Sn could potentially provide the OH_{ads} needed for the re-oxidation of $Ni(OH)_2$ to the active oxyhydroxide sites (Equation 2).

Ni-Sn catalysts have been demonstrated effective in promoting the electrooxidation of methanol, ethanol, and urea, among others, the performance of NiSn towards the GOR is yet to be explored.[29,30] In this work, we investigate the effect of Sn inclusion in Ni nanoparticles supported on carbon nanotubes (CNTs) as a catalyst for the GOR. We analyze how the amount of Sn influences the GOR

kinetics and the oxidation products at different potentials and initial glucose concentrations. Furthermore, we explore the products generated over extended 24-hour reactions at both room temperature and 55 °C. Additionally, we assess the stability of the catalysts through consecutive one-hour electrochemical experiments with electrolyte regeneration between each cycle. Besides, to rationalize the obtained results, density functional theory (DFT) calculations are used to identify the effect of Sn on the $Ni(OH)_2$ structure.

Experimental section

Chemicals

Oleylamine (OAm, 98%), sulfuric acid (H_2SO_4, 98 %), and acetic acid (AA, 99.8%) were purchased from Acros Organics. Lactic acid solution (LA, 90%) was obtained from VWR, and D-gluconic acid aqueous solution (GNA, 50%) from ThermoFisher. Nickel(II) acetylacetonate ($Ni(acac)_2$, 95%), tin(II) acetate ($Sn(OAc)_2$, 95%), tri-n-octylphosphine (TOP, 97%), borane tert-butylamine complex (TBAB, 97%), potassium hydroxide (KOH, 85%), D-(+)-Glucose (99.5%), D-saccharic acid potassium salt (GRA, 98%), D-(-)-Fructose (99%), oxalic acid (OXA, 98%), formic acid (FA, 97%) and Nafion (5 wt% in a mixture of low aliphatic alcohols and water) were obtained from Sigma-Aldrich. Multi-walled carbon nanotubes (MWCNT) were purchased from Carnd-China. Hexane, ethanol, and acetone were of analytical grade and purchased from various sources. MilliQ water was obtained from a Purelab flex from Elga. All reagents and solvents were used without further purification.

Synthesis of $Ni_{0.9}Sn_{0.5}$, $Ni_{0.5}Sn_{0.9}$ and Ni nanoparticles

The synthesis of $Ni_{0.9}Sn_{0.5}$ nanoparticles was adapted from our previous work.[31] Briefly, 224 mg (0.9 mmol) of $Ni(acac)_2$ and 112 mg (0.5 mmol) of $SnCl_2$ were mixed with 20 mL of OAm in a 50 mL three-neck flask and degassed under vacuum at 120 °C for 1 h. Under Ar atmosphere, 5 mL of TOP was introduced. Then the temperature was raised to 230 °C at a rate of 5 °C min^{-1}. Once the solution reached 230 °C, a solution of 2.5 mmol of TBAB in 5 mL of purged OAm was injected. After the injection, the solution turned immediately black indicating the nucleation of Ni–Sn nanocrystals. Then it was allowed to react for 2 h before it was cooled to ambient temperature with a water bath. The product was precipitated with acetone, centrifugated at 7000 rpm for 3 min, and re-dispersed with chloroform. This cleaning cycle was repeated 3 times and the final black product was kept in hexane. To produce the $NiSn_{1.8}$, the ratio Ni/Sn was variated increasing the amount of $SnCl_2$ to 202 mg and reducing the $Ni(OAc)_2$ to 124 mg. On the other hand, Ni nanoparticles were produced without adding $SnCl_2$.

Synthesis of Ni_xSn_y@CNTs

$NiSn_x$@CNTs electrocatalysts were prepared by supporting the particles onto MWCNTs, with a loading amount of 20 %. To prepare the catalyst, a dispersion of $NiSn_x$ ($NiSn_{0.6}$, $NiSn_{1.8}$, or Ni) nanoparticles in

hexane was mixed with a dispersion of MWCNTs in ethanol. The mixture was sonicated for 1 h. Then the product was collected by centrifugation and then re-dispersed in a mixture of acetic acid/ethanol (10 % v/v) to remove surface organic ligands through sonication. Afterward, the catalyst was washed three times with ethanol, dried at 60 °C overnight, and annealed at 300 °C in an Ar atmosphere 1 h.

Characterization

Powder X-ray diffraction (XRD) patterns were collected from the samples supported on a Si substrate on a Bruker-AXS D8 Advanced X-ray diffractometer with Ni-filtered (2 μm thickness) Cu K radiation (λ = 1.5406 Å) operating at 40 kV and 40 mA. The 2θ range was between 20-80°. Scanning electron microscopy (SEM) analysis was conducted with a Zeiss Auriga microscope equipped with an energy-dispersive X-ray spectroscopy (EDS) detector and backscattering electron (BSE) contrast mode, operating at 20 kV. High-resolution transmission electron microscopy (HRTEM) images and scanning transmission electron microscopy (STEM) studies were conducted on an FEI Tecnai F20 field emission gun microscope operated at 200 kV with a point-to-point resolution of 0.19 nm, which was equipped with high angle annular darkfield (HAADF) and a Gatan Quantum electron energy loss spectroscopy (EELS) detector. Atomic resolution aberration-corrected high angle annular dark field scanning transmission electron microscopy (AC-HAADF-STEM) was performed in a double aberration-corrected Thermo Fisher Spectra 300 STEM operated at 300 KeV. The Spectra 300 is equipped with a Super X energy dispersive X-ray spectroscopy (EDS) detector. X-ray photoelectron spectroscopy (XPS) was analyzed on a SPECS system equipped with an Al anode XR50 source operating at 150 W and a Phoibos 150 MCD-9 detector. The Multipak data reduction software (Physical Electronic-PHI, Inc., EE. UU.) was employed for the data process (C 1s peak corrected at binding energy of 284.8 eV). Inductively coupled plasma optical emission spectroscopy (ICP-OES) was conducted using an Agilent system model 5100.

Electrochemical tests

A catalyst ink was prepared by ultrasonically dispersing 6 mg of electrocatalyst, 0.8 mL of isopropanol, 0.2 mL of H_2O, and 50 μL of Nafion. Electrochemical analyses were conducted in an H-type electrochemical cell at room temperature with a BioLogic electrochemical workstation. A three-electrode system was utilized to perform all the tests with a Pt gauze as a counter electrode and a Hg/HgO (KOH saturated) electrode as a reference. The working electrode was prepared by coating a carbon paper (CP), with a surface area of 1 cm^2, with 0.5 mL of the ink using an aerograph to disperse the liquid. The amount of catalyst deposited onto the CP was 3 mg.

All the potentials were converted to reversible hydrogen electrode (RHE) potential following equation (4):

$$E_{RHE} = E_{Hg/HgO} + 0.059 \cdot pH + 0.098 \quad (4)$$

A proton exchange membrane (Nafion 117) was used to separate anode and cathode compartments. The cathode was prepared using a 45 mL solution of 1M KOH, while 45 mL of a glucose solution in 1M KOH was used in the anode. Cyclic voltammetry (CV) and linear sweep voltammetry (LSV) curves were performed at a scan rate of 5 mV/s. Electrochemical impedance spectroscopy (EIS) was carried out from 100 MHz to 0.1 Hz with an amplitude of 5 mV. The electrochemical surface area (ECSA) was established with the double-layer capacitance (C_{dl}), obtained by CV cycles at OCP ± 50 mV at different scan rates (from 5 - 100 mV s^{-1}). Generally, C_{dl} is determined from the linear fit of the current (I) vs the scan rate (v):

$$\mathrm{I} = C_{dl} \cdot v \tag{5}$$

Then, ECSA is calculated by dividing the double-layer capacitance by the specific capacitance (C_s)

$$ECSA = \frac{C_{dl}}{C_{\mathrm{s}}} \tag{6}$$

which is 0.04 mF cm^{-2} based on values reported in alkaline solution.[32]

Chronoamperometry (CA) experiments were conducted for 1 hour at a potential range from 1.35 to 1.6V vs RHE at a concentration of 10 mM glucose in 1M KOH. The same conditions were used, but this time maintaining the applied potential constant at 1.45 V and 1.55 V, while increasing the glucose concentration from 10 mM to 100 mM

Product analysis

Liquid products generated from the glucose electrooxidation were quantified by high-performance liquid chromatography (HPLC) equipped with a Rezex™ ROA-Organic Acid H^+ (8%) column (LC column 300 x 7.8 mm), diode array detector operating at 210 nm and a refractive index detector. The mobile phase consists of a 0.005 N H_2SO_4 solution with a flow rate of 0.2 mL min^{-1} and a temperature of 40 °C. For the HPLC determination, 1 mL of the sample is extracted and diluted with 0.5 mL of 2M H_2SO_4 aqueous solution. FE was calculated with the following equation (7):

$$FE\ (\%) = \frac{n_{e^-} \cdot \mathrm{F} \cdot mol_{\text{product}}}{Q_{\text{total}}} \cdot 100 \tag{7}$$

where F is the faradaic constant (96500 C mol^{-1}), n is the number of transferred electrons based on the balanced half-cell reaction and Q is the total charge passed throughout the experiment.

Selectivity was calculated with the following equation (8):

$$Selectivity\ (\%) = \frac{mols_{\text{product}} \cdot C_{\text{product}}}{mols_{\text{glucose}} \cdot C_{\text{glucose}}} \cdot 100 \tag{8}$$

where $C_{product}$ is the number of carbons of each product, $C_{glucose}$ is the number of carbons that the molecule of glucose has ($C_{glucose}$ = 6), $mols_{product}$ are the mols obtained of each product, and $mols_{glucose}$ are the mols of glucose consumed during the reaction.

DFT analysis

DFT calculations were carried out with the Vienna Ab-initio Simulation Package (VASP).[33,34] The Perdew–Burke–Ernzehof (PBE) functional within generalized gradient approximation (GGA) was chosen to describe the electronic exchange-correlation energies.[35] The projector-augmented-wave (PAW) method was utilized to describe the interaction between the electrons and the ions.[36] For all the geometry optimizations, the cut-off energy was set at 600 eV. The 2×2×1 Monkhorst-Pack k-points were used to sample the Brillouin zone.[37] A mono-layer 3×4×1 $Ni(OH)_2$ (001) model which contains 12 Ni atoms was used to represent the pristine $Ni(OH)_2$ catalysts, while a mono-layer $Ni(OH)_2/SnO_2$ which contains 6 Ni atoms and 6 Sn atoms was chosen to represent the oxidative NiSn alloy system. A vacuum with a 15 Å thickness along the z-axis was inserted to eliminate the periodic interaction of the catalysts. A Hubbard U was specified onto the d orbitals of Ni with an effective U value of 4.00. All atoms could relax until the electronic self-consistency and the ionic relaxation reached the convergence criteria of 10^{-6} eV and 0.01 eV/Å. The adsorption energies for glucose on the surfaces were calculated based on the following equation (9):

$$E_{ads} = E^*_{glucose} - (E^* + E_{glucose}) \quad (9)$$

where $E^*_{glucose}$, E^*, and $E_{glucose}$ are the total energies for glucose adsorbed on the $Ni(OH)_2$ or $Ni(OH)_2/SnO_2$. A more negative E_{ads} means a stronger adsorption.

To determine the effect of SnO_2 on the O-H bond scission in both pristine $Ni(OH)_2$ and $Ni(OH)_2/SnO_2$. The formation energy of H vacancy ($E_{f\text{-}H}$) was calculated according to equation 10:

$$E_{f\text{-}Hv} = E_{slab\text{-}Hv} + 1/2\ E_{H2} - E_{slab} \quad (10)$$

where $E_{slab\text{-}Hv}$, E_{H2}, and E_{slab} are the total energies of structure with an H vacancy, gaseous H_2, and the catalysts without hydrogen vacancy, respectively. A more positive $E_{f\text{-}Hv}$ means a more difficult O-H scission.

Results and discussion

Catalyst preparation and characterization

NiSn-based catalysts supported on carbon nanotubes ($NiSn_y$/CNT) were produced in four steps (Scheme 2, see details in the Experimental section). First, colloidal NiSn nanoparticles were synthesized from the simultaneous co-reduction at 230 °C of the two metal precursors, $Sn(Oac)_2$ and $Ni(acac)_2$, with

borane tert-butylamine (TBAB) within a mixture of oleylamine (OAm) and trioctylphosphine (TOP), used as solvents and stabilizers. NiSn particles with two Ni/Sn precursor ratios, $NiSn_{1.8}$ and $NiSn_{0.6}$, were produced. Additionally, as a reference, a pure Ni sample was also produced in the same conditions. In a second step, to maximize the electrocatalyst electrical conductivity and minimize the aggregation of the NiSn particles, they were dispersed on the surface of multi-walled CNTs. Finally, in a third and fourth step, ligands were removed using a diluted AA solution and the material was annealed at 300 °C for 1 h under an inert atmosphere.

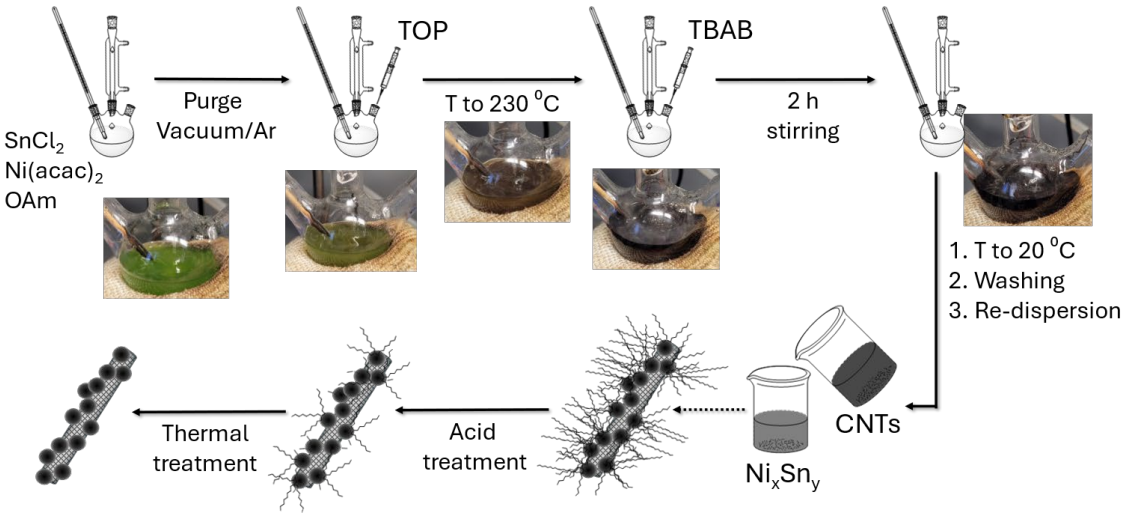

Scheme 2. Schematic diagram of the preparation of the NiSn-based catalyst

Figure 1a-f shows representative transmission electron microscopy (TEM) and scanning TEM in high-angle annular dark-field (STEM-HAADF) images of the different catalysts. The Ni particles in Ni/CNT appear very small and are distributed along the CNTs with an undefined geometry. With the introduction of Sn, the particle geometry becomes more regular. While $NiSn_{0.6}$ particles have a spheroidal shape with a large size and shape distribution, $NiSn_{1.8}$ particles are slightly smaller and show a more homogeneous spherical geometry. XRD pattern (Figure 1g) of Ni/CNTs shows no metal-related XRD peaks, which is consistent with an amorphous lattice. Only the XRD pattern of the carbon nanotubes with a main peak at about $2\theta \approx 25°$ is observed. In contrast, the XRD patterns of the two $NiSn_y$/CNT catalysts produced show the presence of the orthorhombic Ni_3Sn_2 crystallographic phase. In both $NiSn_y$/CNT samples, bands around $2\theta \approx 28°$ and $2\theta \approx 34°$ can be appreciated, which coincide with the main peaks of the SnO_2 structure. The presence of both metals was confirmed through inductively coupled plasma mass spectrometry (ICP-OES) and scanning electron microscopy coupled with energy-dispersive X-ray spectroscopy (SEM-EDS, Figure S1). The Ni/Sn ratios of the two $NiSn_y$/CNT samples measured by ICP-OES were $NiSn_{0.8}$ and $NiSn_{1.5}$, which slightly differ from the nominal metal ratios used. Nevertheless, we will rely on the nominal metal ratio to refer to the two different materials.

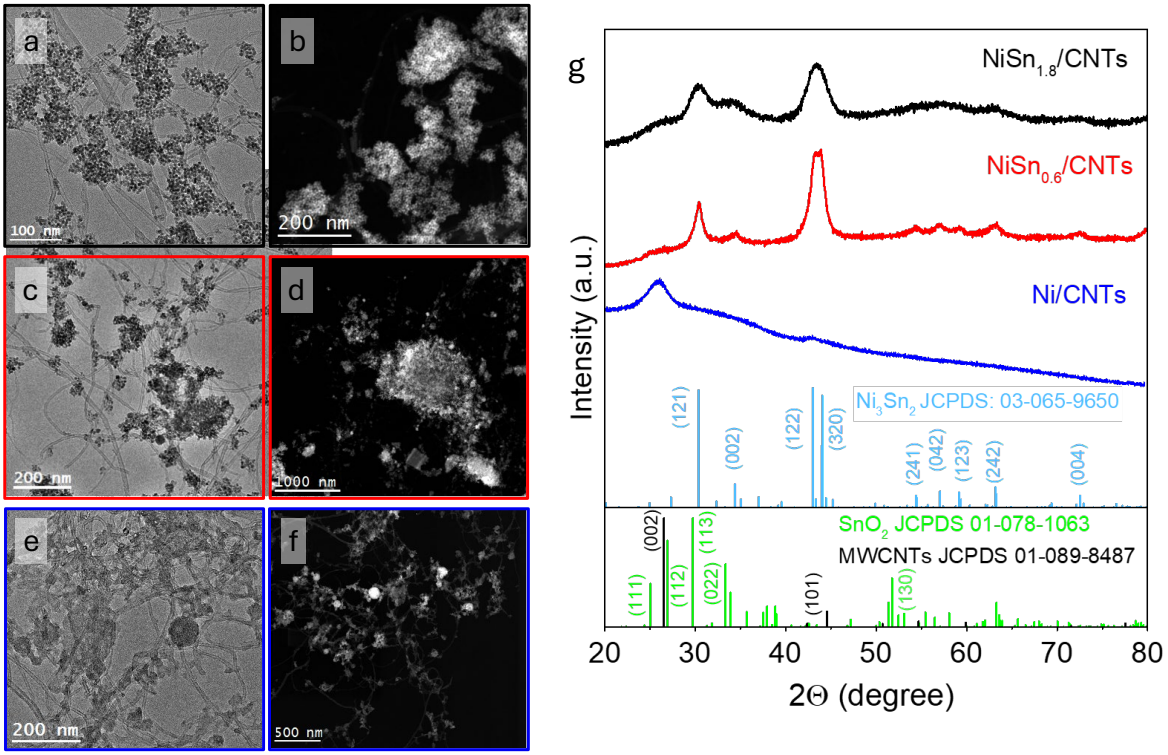

Figure 1. (a-f) Representative TEM (a, c, e) and STEM-HAADF (b, d, e) micrographs of $NiSn_{1.8}$/CNT (a,b), $NiSn_{0.6}$/CNT (c, d) and Ni/CNT (e, f) catalysts. (g) XRD patterns of $NiSn_{1.8}$/CNT (black line), $NiSn_{0.6}$/CNT (red line), and Ni/CNT (blue line) catalysts.

Figure 2a-b shows an aberration-corrected (AC) STEM-HAADF image of the $NiSn_{0.6}$/CNT sample. The power spectrum analysis confirms the presence of the Ni_3Sn_2 phase, characterized by an orthorhombic crystal structure within the Pnm space group. Moreover, atomic resolution AC STEM-HAADF images display a SnO_2 shell surrounding the Ni_3Sn_2 core, with an orthorhombic structure belonging to the Pbcn space group. Upon further examination of the atomic plane frequencies obtained from the fast Fourier transform (FFT) spectra calculated using STEM-HAADF images (specifically, the bottom right panel in Figure 2a), we observed additional frequency spots corresponding to atomic planes associated with SnO_2. After filtering out these frequencies related to SnO_2 and aligning them with the Ni_3Sn_2 core lattice fringes, we evidenced that the SnO_2 shell exhibits a discontinuous morphology, as clearly depicted in the frequency-filtered map shown in Figure 2b. The thickness of the SnO_2 shell is close to 2 nm. Frequency-filtered maps of a single nanoparticle (Figure 2b) and EDX maps of a particle's ensemble (Figure 2c) corroborate the core-shell structure. HRTEM analysis of the $NiSn_{1.8}$ nanoparticles displays a similar core-shell structure (Figure S2), showing a core crystallizing in the Ni_3Sn_2 orthorhombic phase and a similarly thick SnO_2 shell. The similar shell thickness despite the higher Sn amount is consistent with the smaller size of the $NiSn_{1.8}$ cores. HAADF-STEM coupled with electron energy loss spectroscopy (STEM-EELS) analysis of the $NiSn_y$/CNT (Figures S3 and S4) shows that Sn is homogeneously distributed throughout the sample, while Ni is concentrated within the center of the particles (core) and the O is

mainly found in the nanoparticles shell. In Ni/CNT, oxygen and nickel are equally distributed, showing full oxidation of the nickel nanostructures (Figure S5).

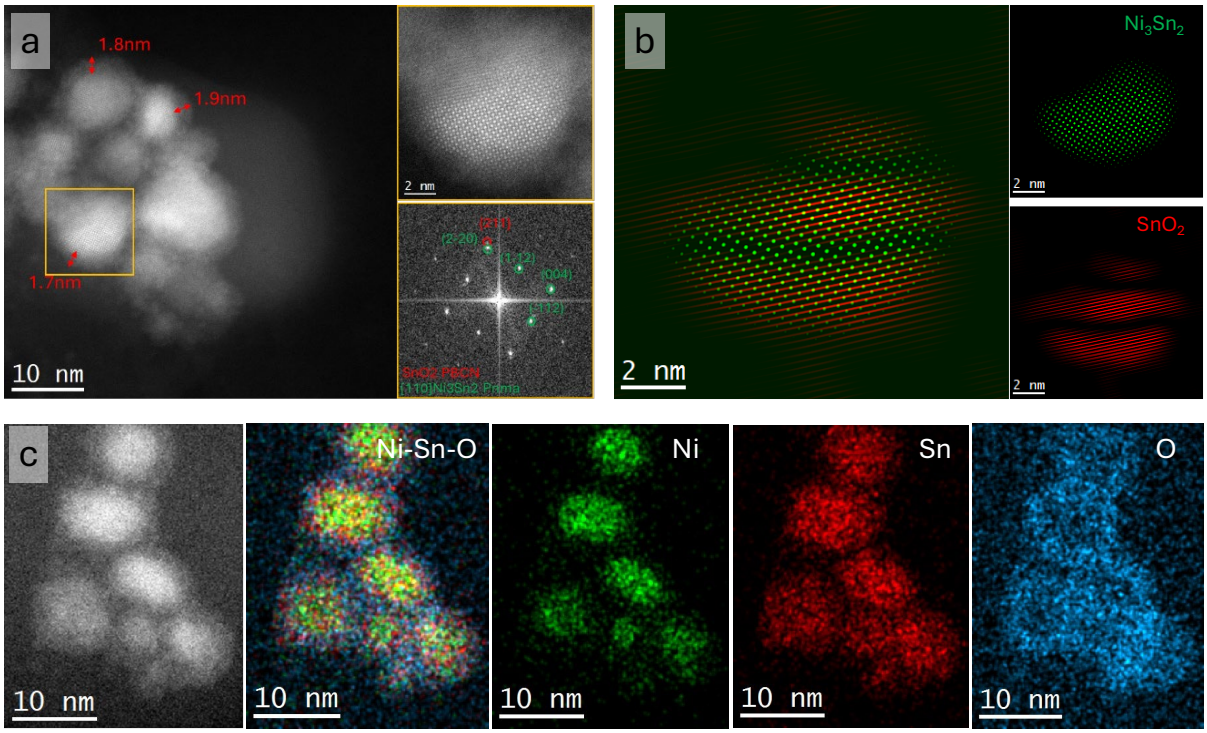

Figure 2. (a) Z-contrast AC STEM-HAADF micrograph of $NiSn_{0.6}$ nanoparticles and detail of the orange squared region and its corresponding FFT. (b) Frequency filtered map of the nanoparticle highlighted in (a) by the orange box showing the Ni_3Sn_2 core in green and SnO_2 shell in red. (c) EDX elemental maps of $NiSn_{0.6}$ particles showing the Ni (green), Sn (red), and O (blue) distributions.

The high-resolution Ni 2p X-ray photoelectron spectroscopy (XPS) spectrum of $NiSn_{0.6}$/CNT shows two doublets at 853.0 eV ($2p_{3/2}$) and 856.7 eV ($2p_{3/2}$), corresponding to Ni(0)and Ni(II) oxidation states, respectively (Figure S6a). The Ni(II) chemical environment, which accounts for about 56% of the total Ni detected on the $NiSn_{0.6}$/CNT surface, is generated during the acid treatment. Likewise, Sn exists in two chemical states, Sn(0) at 485 eV ($3d_{5/2}$) and Sn(IV) at 487 eV ($3d_{5/2}$). The Sn(IV) accounts for about 79% of the total Sn detected by XPS. The Ni/Sn atomic ratio provided by XPS is Ni/Sn ≈ 0.1, which is consistent with the Sn surface segregation and the formation of the SnO_2 shell on the Ni_3Sn_2 particle surface, as observed by atomic resolution AC HAADF STEM, STEM-EDX, and STEM-EELS analyses. Similar results were obtained for the $NiSn_{1.8}$/CNT sample (Figure S6b). In this case, Ni(0) and Ni(II) oxidation states account for about 47% and 53% of the total Ni, respectively. Besides, Sn(0) and Sn(IV) account for about 10% and 90% of the total Sn. The Ni/Sn atomic ratio provided by XPS in this sample is Ni/Sn ≈ 0.05, consistent with the higher amount of Sn introduced in this material, the Sn surface segregation, and the formation of the SnO_2 shell on the Ni_3Sn_2 particle surface, as observed by HRTEM, STEM-EDX and STEM-EELS analyses. On the other hand, the Ni 2p XPS spectrum of the Ni/CNT sample

(Figure S7) confirms a unique oxidation state (Ni(II)) associated with the small size of the Ni particles in this sample.

Electrochemical characterization

The electrochemical properties of the Ni-based catalysts towards GOR were evaluated using a double-compartment H-cell, with a conventional three-electrode configuration (see details in the SI). Electrodes were fabricated onto a 1 x 1 cm carbon paper (CP) substrate via airbrushing using an ink containing 3 mg of catalyst, 0.75 mL of ethanol, 0.2 mL of Milli-Q water, and 50 µL of Nafion (Figure S8). Despite its lower conductivity and smaller surface area compared to Ni foam, CP was selected as support to remove a potential role of the Ni support on the GOR reaction.

Linear sweep voltammetry (LSV) in the potential range of 1.0 to 1.8 V vs RHE was first conducted in 1 M of KOH at a scan rate of 5 mV s^{-1} (Figure 3a). LSV curves show a peak between 1.3 V and 1.5 V corresponding to the Ni^0/Ni^{2+} oxidation to Ni^{3+} (NiOOH). At potentials higher than 1.6 V, LSV voltammograms display an increase in intensity associated with the OER. The larger Ni oxidation current obtained for Ni/CNTs and $NiSn_{0.6}$/CNT compared with $NiSn_{1.8}$/CNT is consistent with the lower Ni amount of the latter. The larger Ni oxidation current obtained with the $NiSn_{0.6}$/CNT electrode, compared to the Ni/CNT, can be attributed to two factors. First, in the bimetallic samples, nickel is found in both Ni^0 and Ni^{2+} states, implying that part of the oxidation to Ni^{3+} involves three electrons (Ni^0 to Ni^{3+}). In contrast, all the Ni within Ni/CNTs is found as Ni^{2+}, thus involving only one electron (Ni^{2+} to Ni^{3+}). XPS analysis of the electrodes after the electrochemical experiment (Figure S9) reveals that the metallic Ni peaks in the bimetallic samples have disappeared, indicating complete oxidation of nickel during the LSV. Besides, the oxyhydroxide formation involves the reaction with OH^- molecules in solution, which is potentially enhanced by the oxophilic nature of Sn. In this direction, Tafel plots confirm the NiSn alloy to promote the kinetics of NiOOH formation (Figure S10a).

The electrocatalytic GOR activity was evaluated by adding 10 mM of glucose to the 1 M KOH solution. LSV curves of the electrodes in the presence of glucose (Figure 3b) display three distinct regions: (1) a minor rise in current between 1.1 V and 1.35 V, associated with the formation of Ni^{3+} species, followed by (2) an abrupt boost at approximately 1.35 V, coinciding with the Ni oxidation to Ni^{3+}, and (3) a subsequent current surge at potentials higher than 1.55 V, where the contribution of the OER becomes significant. As will be discussed later in the manuscript, glucose conversion at potentials below 1.35 V is almost negligible, which confirms NiOOH species are the truly active catalysts. XPS analysis of the material after the LSV curves confirms the presence of Ni^{3+} (Figure S10). The current densities in the 1.1-1.35 V region match well the amount of Ni within each material, Ni/CNT > $NiSn_{0.6}$/CNT > $NiSn_{1.8}$/CNT. The current density in region 2 (1.35 V - 1.6 V) reflects the GOR electrocatalytic activity of

the materials. Both the onset potential and the steepness of the slope improve with the tin content. The GOR Tafel plots (Figure 3c) in this second region confirm that the kinetics are faster in $NiSn_{1.8}$/CNT > $NiSn_{0.6}$/CNT > Ni/CNT. As the applied potentials increase, mass transport becomes the limiting step of the process. Desorbed products from the electrode surface hinder the arrival of new glucose molecules, leading to a saturation of the current displayed in the voltammogram. The saturation current of the $NiSn_{1.8}$/CNTs catalyst remains significantly lower than that of the other two materials owing to the lower amount of Ni. Meanwhile, in the Ni/CNT, given that the reaction proceeds at a slower rate compared to bimetallic compounds, it is necessary to apply higher potentials to augment the GOR rate and attain electrode surface saturation. Increasing the glucose concentration prevents current saturation by alleviating reactant diffusion limitations. Notably, $NiSn_{0.6}$/CNT exhibits its peak GOR activity in 100 mM of glucose, as observed by LSV (Figure 3d) and the Tafel plot (Figure S10b).

Cyclic voltammetry (CV) in the range between 1.0 V and 1.8 V of the electrodes within a 1 M KOH solution shows the pair redox Ni^{2+}/Ni^{3+} at oxidation potentials between 1.3-1.5 V and reduction potentials between 1.3-1.05 V (Figure 3e). When adding 100 mM glucose, a significant increase in current associated with the GOR is observed for all the samples, and no reduction peak is detected. As displayed in equation 3, the glucose oxidation induces the reduction of NiOOH to $Ni(OH)_2$. All the NiOOH species formed are immediately reduced upon glucose interaction. Thus during the reduction process, all species are already reduced, which explains the absence of the reduction peak. Extending the potential window down to 0.1 V (Figure S11), with and without glucose, no additional oxidative peaks are obtained. Nevertheless, during the reduction process in 1 M KOH, an extra peak is observed at 0.5 - 0.7 V, corresponding to the reduction of the oxygen generated during the OER at high potentials. Since, in the presence of glucose, the GOR activity predominates over OER for the as-prepared electrocatalysts within the measured potential range, hardly any current variation associated with the oxygen reduction reaction is observed. The electrochemical impedance spectroscopy (EIS) data in Figure 3f indicate that $NiSn_{0.6}$/CNT exhibited the lowest charge-transfer resistance, confirming it as the most efficient GOR catalyst among the three tested materials.

The relative electrochemically active surface area (ECSA) was estimated by double-layer capacitance (C_{dl}) measurements (Equations 5 and 6). Capacitances for the as-prepared catalysts are compared in Figure S12. Results show that the calculated capacitance follows a trend Ni/CNT > $NiSn_{1.8}$/CNT > $NiSn_{0.6}$/CNT. The calculated ECSA values indicate that Ni/CNT has the highest electrochemical surface area (205 cm^2), followed by $NiSn_{1.8}$ (122.5 cm^2) and $NiSn_{0.6}$ (60 cm^2), which is consistent with the different sizes of the Ni-based particles, but it is inversely proportional to the kinetics of the GOR process. This suggests that the activity of the prepared materials is closely related not to the exposed active sites but to their intrinsic activity.

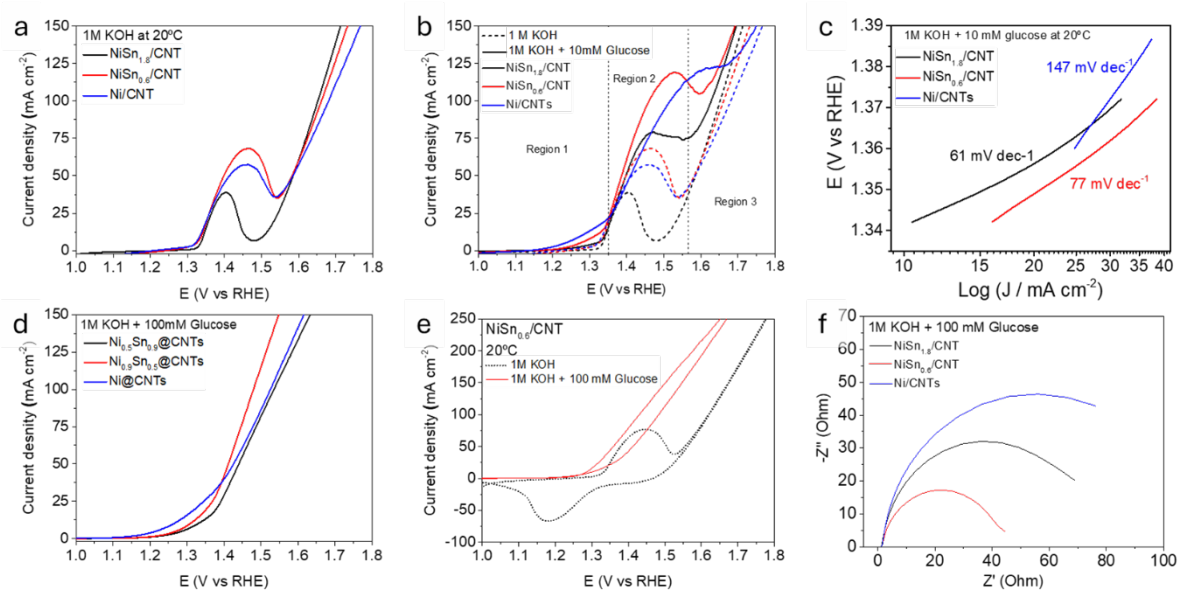

Figure 3. (a-d) LSV voltammograms in 1 M KOH aqueous solution (a), LSV voltammograms and Tafel slopes in 1 M KOH + 10 mM glucose aqueous solution (b, c) and LSV voltammograms in 1 M KOH + 100 mM glucose aqueous solution (d) using $NiSn_{1.8}$/CNT (black line), $NiSn_{0.6}$/CNT (red line) and Ni/CNT (blue line) catalysts. (e) CV voltammograms of $NiSn_{0.6}$/CNT in 1 M KOH (black dotted line) and (red solid line) 1 M KOH + 100 mM glucose. (f) Nyquist plots in 1 M KOH + 100 mM glucose aqueous solution of $NiSn_{1.8}$/CNT (black line), $NiSn_{0.6}$/CNT (red line), and Ni/CNT (blue line) catalysts.

In the Faradaic region, the potential difference between the oxidation and reduction peaks of $Ni(OH)_2 \leftrightarrow NiOOH$ is directly correlated with the electron transfer kinetics between the electrode surface and the active centers, which indicates whether the reaction is kinetically favorable.[38] Comparing the value of 0.25 V, obtained for $NiSn_{0.6}$, with the values of 0.3 V and 0.18 V for Ni and $NiSn_{1.8}$, respectively (Figure S13), it is evident that the incorporation of Sn improves the reaction kinetics of $Ni(OH)_2 \leftrightarrow NiOOH$.

The surface coverage of $Ni(OH)_2$/NiOOH redox species (Γ*) is another key kinetic parameter for evaluating and comparing the performance of different materials. This parameter provides information about the amount of NiOOH active sites available on the surface, which are crucial for electrochemical reactions. The Γ* can be determined from the linear fit of the anodic peak current (I_a) with the sweep rate (v) from 10-80 mV s^{-1} (Figures S14)

$$I_{ac} = \left(\frac{n^2F^2}{4RT}\right) A\Gamma^* \nu \qquad (11)$$

where F is the Faraday constant (96485 C mol^{-1}), n is the number of transferred electrons (n=1), T is the temperature (295 K), R is the gas constant (8.314 J K^{-1} $mol^{-1)}$ and A is the geometric surface area of the electrode (1 cm^2). The Γ* value for $NiSn_{0.6}$ electrodes, as obtained from the forward scans, was

2.9×10^{-6} mol cm^{-2} (Figure 4e), which is slightly higher than the Γ* value for Ni at 2.7×10^{-6} mol cm^{-2} and for $NiSn_{1.8}$ at 1.9×10^{-6} mol cm^{-2}. A higher Γ* value indicates a greater density of active sites, which can translate to a higher charge storage capacity and improved efficiency in electron transfer.

Since proton diffusivity is generally the rate-limiting step controlling the $Ni(OH)_2 \leftrightarrow NiOOH$ redox reaction for Ni-based electrodes,[39] we decided to calculate the proton diffusivity (D) within the electrodes using the simplified form of the Randles–Sevcik equation (12):

$$I_{ac} = 2{,}69 \cdot 10^5 \, n^{3/2} A \, D^{1/2} C v^{1/2} \quad (12)$$

n represents the number of electrons transferred in the redox reaction, while A denotes the electrode area. The diffusion coefficient of the redox species is indicated by D, the concentration of the redox species is given by C, and v stands for the scan rate. The results for the proton diffusion coefficient indicate that diffusion in the $NiSn_{0.6}$ electrode (3.81×10^{-7} cm^2 s^{-1}) is faster than in Ni/CNT (3.12×10^{-7} cm^2 s^{-1}) and $NiSn_{1.8}$/CNT (1.86×10^{-7} cm^2 s^{-1}).

The TOF values were deduced from the mass of the catalyst added to the electrode

$$\mathrm{TOF} = \left(\frac{\mathrm{J\,A}}{\mathrm{n\,F\,m}}\right) \quad (13)$$

where F is the Faraday constant (96485 C mol^{-1}), n is the number of transferred electrons, m is the number of moles of catalyst involved in the reaction, J is the current density and A is the geometric surface area of the electrode (1 cm^2). A TOF value of 0.044 s^{-1} was obtained for $NiSn_{0,6}$ at 1.45 V in the presence of glucose, while $NiSn_{1,8}$ and Ni showed TOF values of 0.035 s^{-1} and 0.007 s^{-1}, respectively. This TOF value indicates that the active sites in NiSn catalysts are more efficient compared to the monometallic compound, as the reaction kinetics are faster despite a lower ECSA value.

The glucose electrochemical conversion was further studied using chronoamperometry (CA) measurements conducted for 1 h at room temperature. The obtained products were identified and quantified using HPLC. The electrocatalysis was initially carried out with a constant glucose concentration of 10 mM, while varying the working potential within the range from 1.35 to 1.6 V. At potentials lower than 1.35 V, a very low glucose conversion (< 5%) was achieved. Beyond 1.60 V, there is strong competition with the OER, particularly as glucose is being consumed and its concentration decreases, thereby reducing the GOR FE. In the voltage range 1.35-1.6 V, FA, and OXA were the only GOR products, with FA being the predominant one for the three catalysts. This result points to glucose being mainly converted throughout the C-C bond cleavage pathway. Considering the two identified products, the total FE (calculated by Equation 7) is below 100% in the entire potential range tested (Figure 4a-c). We attribute this discrepancy to the overoxidation of the generated FA to CO_2 which was in turn converted to carbonate within the alkaline solution. This was confirmed when 2M sulfuric acid

was added to the electrolyte solution after 1h GOR and a clear effervescence, due to the conversion of carbonates to CO_2, was observed. The FA oxidation was intensified as the applied potential was increased. Thus, the FE for FA gradually decreased with the working potential, even in the range where no competition with OER was expected. The $NiSn_{0.6}$/CNT electrode was the most active when considering LSV curves, but it provided the lowest glucose conversion and the lowest FA selectivities. This is attributed to the faster FA oxidation in this material, which reduces the overall GOR and the GOR-to-FA selectivity.

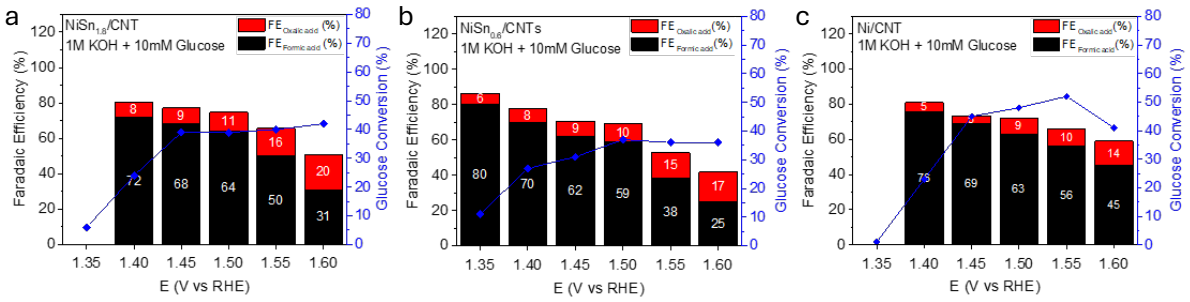

Figure 4. FE of the GOR to FA and OXA using $NiSn_{1.8}$/CNT (a), $NiSn_{0.6}$/CNT (b), and Ni/CNT (c) as electrodes at applied potentials from 1.40 to 1.60 V in 1M KOH and 10 mM glucose for 1h.

Figure 5a-b presents the characterization of the $NiSn_{0,6}$/CNT sample after GOR, conducted at a potential of 1.45 V vs. RHE in 1M KOH and 10 mM glucose. The power spectrum analysis and atomic-resolution AC STEM-HAADF images reveal the presence of both the Ni_3Sn_2 core phase and the SnO_2 shell, with their crystalline structures preserved post-reaction. Furthermore, STEM-EELS analysis (Figure 5c) shows that, following the reaction, Sn remains predominantly localized in the nanoparticle core and the thin oxide shell, consistent with its pre-reaction state. However, a faint signal is also detected throughout the material, suggesting the presence of dispersed Sn atoms across the entire sample. In contrast, nickel is found in large concentrations both at the core and also forming an oxide matrix surrounding the particles, along with small pure Ni precipitates, as indicated by the stronger Ni signal. This surface nickel oxide formation is attributed to the generation of NiOOH during the reaction, highlighting the material's transformation under catalytic conditions.

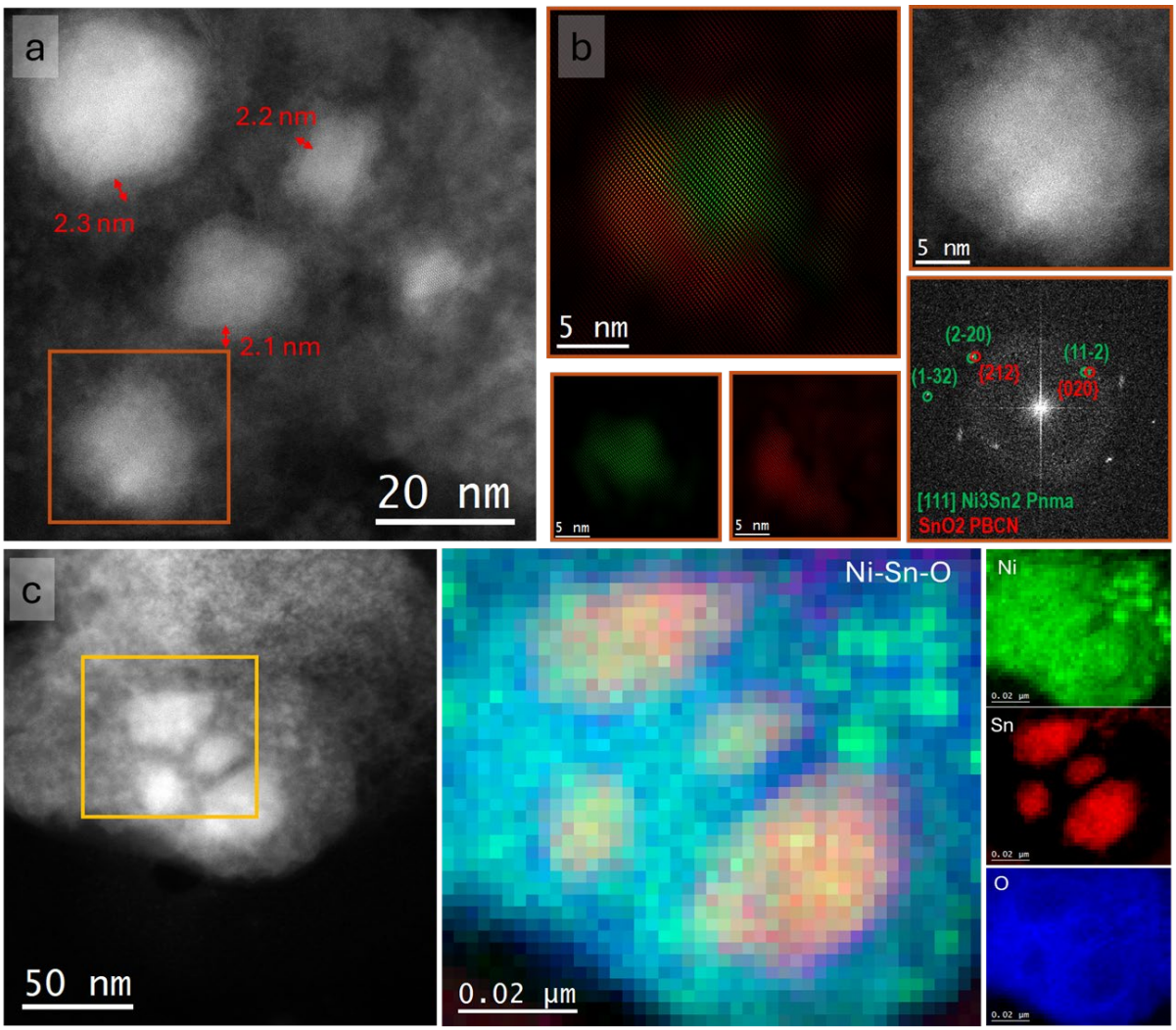

Figure 5. Characterization of $NiSn_{0.6}$ nanoparticles after being used as catalysts in the GOR applying a potential of 1.45 V vs. RHE for 1 h in 1M KOH and 10 mM glucose. (a) Z-contrast AC STEM-HAADF micrograph of the nanoparticles and detail of the orange squared region and its corresponding FFT. (b) Frequency filtered map of the nanoparticle highlighted in (a) by the orange box showing the Ni_3Sn_2 core in green and SnO_2 shell in red. (c) EDX elemental maps of $NiSn_{0.6}$ particles showing the Ni (green), Sn (red), and O (blue) distributions.

The GOR catalytic activity is strongly dependent on glucose concentration. To maximize GOR and minimize FA overoxidation, the potential was set at 1.45 V and the glucose concentration was increased from 10 mM to 100 mM. As depicted in Figure 6a, the FE for FA production increases with the amount of glucose in the solution. At a higher glucose concentration, pristine glucose molecules faster replace the generated FA, which is thus less susceptible to being overoxidated. The $NiSn_{0.6}$/CNT reaches the maximum FA FE (93 %) at 100 mM of glucose and demonstrates to be more selective than $NiSn_{1.8}$/CNT (83 %) and Ni/CNT (84 %) in the same reaction conditions (Figure S15). This FE value for FA is one of the largest values reported and the highest for a Ni-based catalyst (Table S1). At a higher

applied potential of 1.55 V (Figure 6b), the FE for FA also increases with the glucose concentrations, but it decreases in comparison to the results obtained at a lower applied potential due to FA overoxidation. Besides, although the activity for GOR is enhanced using the bimetallic $NiSn_x$/CNT catalysts, the FE at higher potentials for FA is Ni (83%) > $NiSn_{1.8}$ (81%) > $NiSn_{0.6}$. (76%).

As previously mentioned, the C-C cleavage oxidation process competes with the non-Faradaic degradation process. As seen in Scheme 1, under basic conditions, glucose can convert to fructose and subsequently form various compounds such as LA, TA, or AA. This degradation occurs within the bulk of the electrolyte, distinct from the oxidative process occurring at the electrode surface. The overall product selectivity was calculated based on a carbon balance (see details in the Experimental section, Equation 8), which accounts for the glucose consumed in the process and, therefore, includes the products obtained in both the gas and liquid phases. The results show that the non-Faradaic glucose degradation pathway is promoted when the glucose initial concentration is increased, as evidenced by the higher proportion of fructose detected. Additionally, AA is obtained, which has not been widely reported as a product of GOR. Increasing the applied potential, a minor overall selectivity is obtained (Figure 6b), particularly at lower concentrations, due to increased carbonate production. Furthermore, the observed proportion of fructose diminishes with the applied potential, which is attributed to the accelerated GOR, resulting in less remaining unreacted glucose.

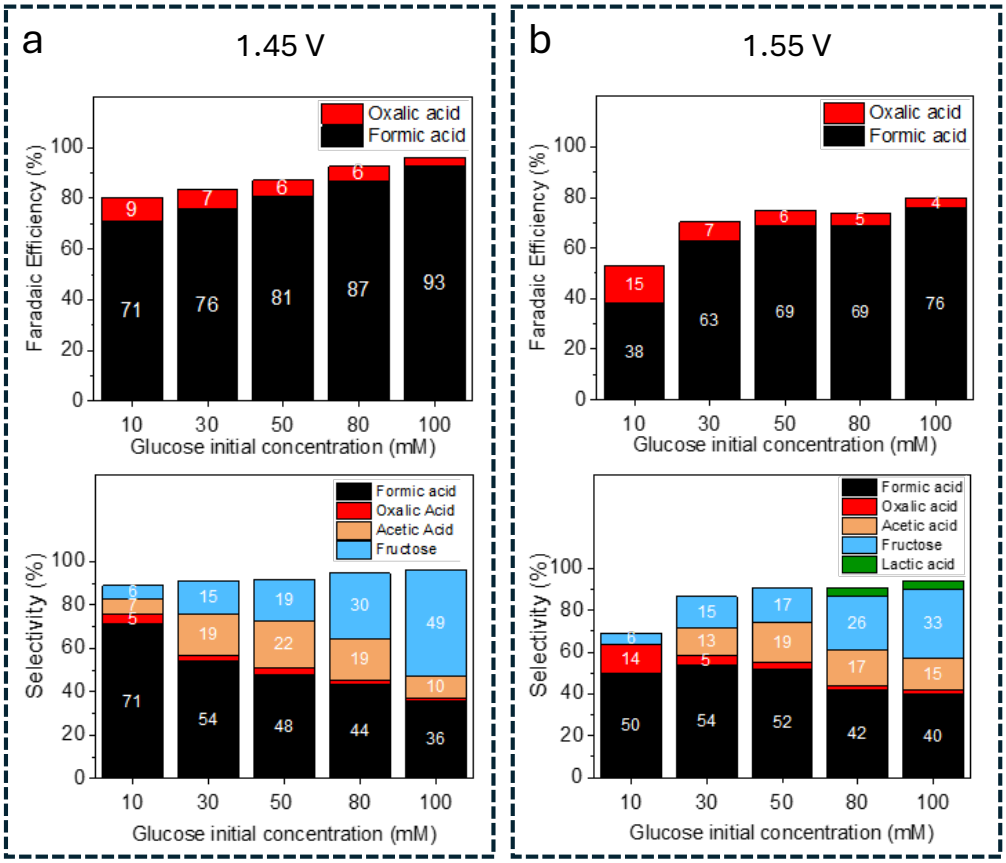

Figure 6. FE (top) and selectivity (bottom) of the products obtained during GOR at applied potentials of 1.45 V (a) and 1.55 V (b) using a $NiSn_{0.6}$/CNT electrode. GOR was performed for 1h at 20 °C in 1M KOH and increasing glucose concentration from 10 to 100 mM.

Most previous works show the results obtained after relatively short reaction times to minimize the glucose conversion by non-Faradaic processes. To evaluate this aspect, a long-term experiment was performed to study how glucose oxidation varies over time (Figure 7). The electrocatalytic reaction was carried out for 24 h at an applied potential of 1.45V and an initial glucose concentration of 30 mM to reduce the overoxidation of FA while also minimizing glucose degradation. At ambient temperature, the FE for FA decreases over time, as the declining glucose concentration leads to overoxidation of the generated FA (Figure 7a). Consequently, a decrease in the selectivity of FA is observed. On the other hand, the selectivity towards AA increases over time, eventually surpassing that of FA. The same experiments were conducted at a temperature of 55°C to enhance the reaction kinetics. Initially, the reaction was performed at a potential of 1.35 V (Figure 7b). At 55°C, unlike at room temperature, a significant consumption of glucose was observed. After 1 hour, the maximum FE value obtained was 94%, although a similar decrease over time was observed. At this potential, a higher selectivity for LA was evident. Elevated temperatures accelerate the kinetics of glucose oxidation to FA but also promote the degradation process. Conversely, at a higher potential of 1.45 V and elevated temperature (55°C), the decrease in FA is more rapid, as is the oxidation of LA, resulting in a higher amount of AA (Figure 6c).

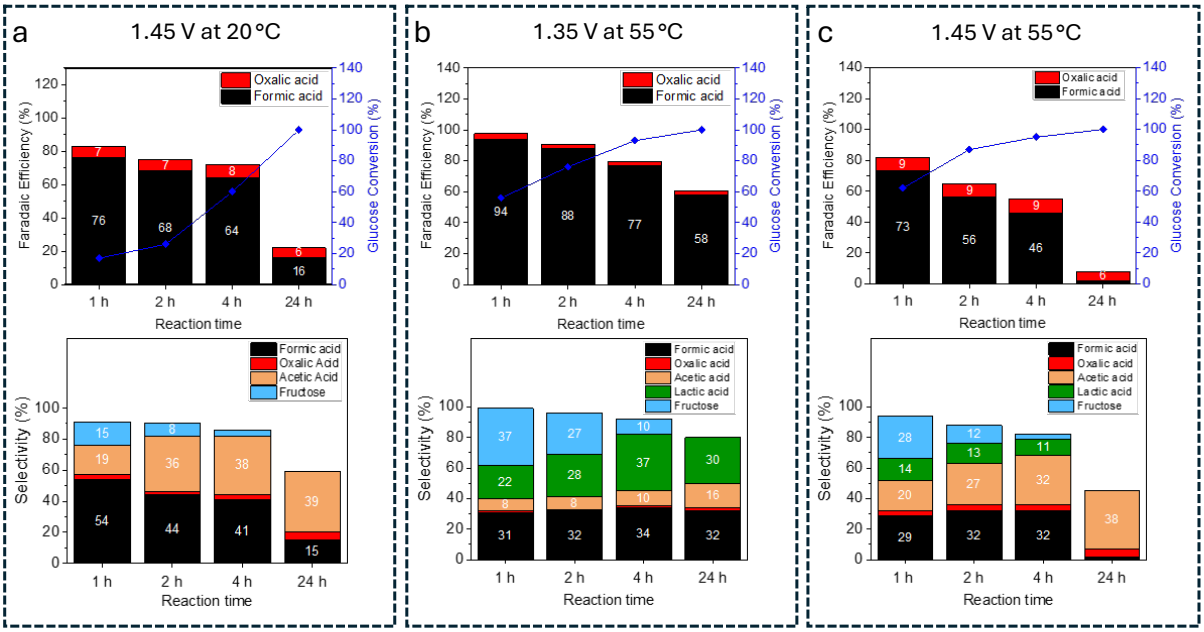

Figure 7. FE and glucose conversion (top) and selectivity (bottom) of products obtained during GOR using $NiSn_{0.6}$/CNT as the electrode in 1M KOH and 30 mM glucose for 24 h. The different experiments were carried out at 1.45 V at 20 °C (a), 1.35 V at 55 °C (b), and 1.45 V at 55 °C (c).

The stability of $NiSn_{0.6}$/CNT under GOR conditions was evaluated through 5 subsequent cycles of CA, each lasting 1 hour in a solution of 1M KOH and 10 mM glucose (Figure S16). After each experiment, the electrolyte was replaced with the same amount of reactant. It is observed that the decrease in the CA curves is solely due to glucose consumption, as each new cycle starts with the same current value. If there were any deactivation of the material, a progressive or total decrease would be observed at the beginning of each cycle. The glucose consumption and formate production in each cycle were analyzed by HPLC (Figure S17) and, at the end of each cycle, both remained constant, indicating that the activity of the catalyst did not decrease with each reaction. The observation is consistent with the post-catalysis characterization results, previously discussed, which show no loss of Ni or Sn after the GOR. This confirms that the NiSn alloy is stable under GOR operation.

DFT calculations

To gain insight into the role of Sn on the GOR over the Ni surface, DFT calculations were conducted. The adsorption energy of glucose on pure $Ni(OH)_2$ and on $Ni(OH)_2$ sites near a Sn atom was first calculated. The top-view and side-view structures of the optimized pristine $Ni(OH)_2$ and the Sn-containing $Ni(OH)_2$, along with the corresponding adsorption structures of glucose, are shown in Figure 8a,b. Calculations revealed that, in absolute value, the adsorption energy of glucose on $Ni(OH)_2$, -0.22 eV increased with the introduction of Sn, up to -0.34 eV. As shown in Figure 8c, the spin density difference between spin-up and spin-down electrons decreased from 0.82 eV to 0.76 eV after introducing Sn to $Ni(OH)_2$. The reduced antiferromagnetic spintronics indicates an improved electroconductivity in the oxidative Sn-containing $Ni(OH)_2$ alloy, which explains the variation in activation energy compared to pristine $Ni(OH)_2$. Besides, to determine the effect of the SnO_2 shell on the catalytic activity of $Ni(OH)_2$, the process of gaining effective oxidative NiOOH intermediate through $Ni(OH)_2$ was analyzed (Figure 8d,e). The $E_{f\text{-}Hv}$ of the pristine $Ni(OH)_2$, which represents the transformation of $Ni(OH)_2$ to NiOOH, is as large as 2.03 eV. In contrast, in the $Ni(OH)_2/SnO_2$ composite, it decreases to 1.06 eV. A more positive $E_{f\text{-}Hv}$ implies the O-H scission is less favored. Thus, overall, the presence of Sn/SnO_2 not only enhances glucose adsorption by modulating the antiferromagnetic spintronics of Ni but also promotes the formation of the active species NiOOH.

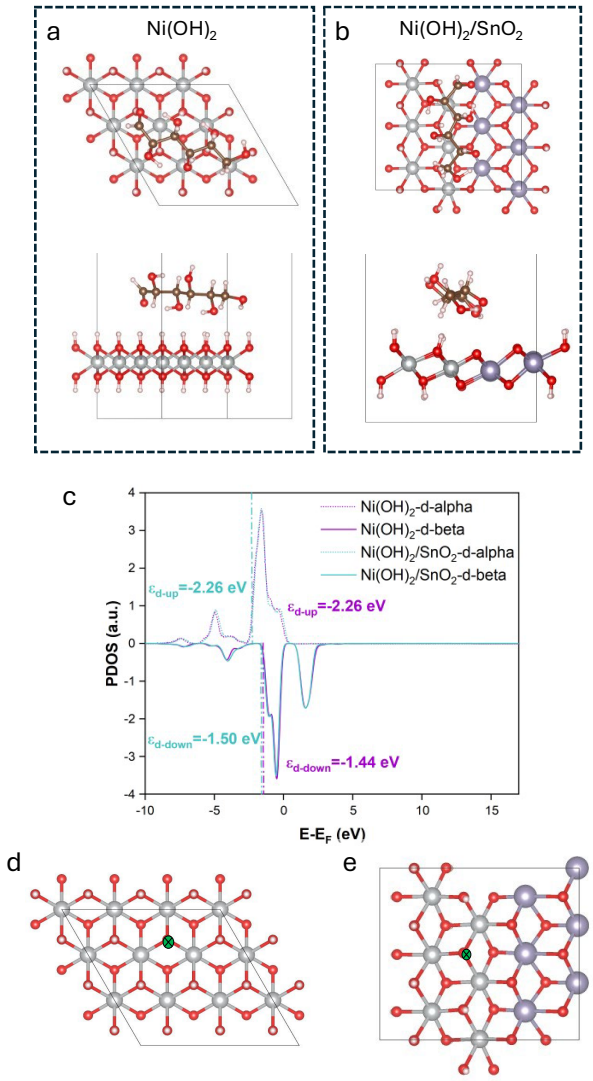

Figure 8. (a,b) Top and side views of the optimized structures of glucose adsorption on $Ni(OH)_2$ (a) and Sn-$Ni(OH)_2$ (b) surface. H (small white), C (small brown), O (small red), Ni (big white), and Sn (big purple). (c) Partial density of states (PDOS) curves of the d-orbital electrons of Ni in $Ni(OH)_2$ and oxidative Sn-$Ni(OH)_2$. (d,e) Top-view of the deprotonation process on $Ni(OH)_2$ surface (d) and oxidative $Ni(OH)_2/SnO_2$ composite (e).

Conclusions

In summary, we detailed the synthesis of $NiSn_x$ nanoparticles via colloidal reduction and their subsequent support on CNTs. Characterization revealed the $NiSn_x$ particles to display a core-shell $Ni_3Sn_2@SnO_2$ architecture, with a porous SnO_2 shell and smaller and more regularly shaped cores observed at higher Sn concentrations. $NiSn_x$/CNT catalysts exhibited enhanced GOR performance, displaying improved kinetics with increasing Sn concentration and higher activity with greater Ni content. Notably, $NiSn_{0.6}$/CNT demonstrated superior electrochemical performance compared to both $NiSn_{1.8}$/CNT and Ni/CNT. Furthermore, the analysis of the oxidation products highlighted the excellent

performance of the $NiSn_{0.6}$/CNT catalyst, achieving a maximum FE of 93% for FA at 1.45 V vs RHE. We observed that at higher potentials and lower concentrations, FA overoxidation to carbonates occurs, reducing the total FE. Higher glucose concentrations mitigate FA overoxidation but increase competition with glucose degradation in basic conditions. Consequently, at high concentrations, FA selectivity decreases, while AA and LA production increases. Enhanced selectivity for these compounds is also observed with longer reaction times and higher temperatures. Even though achieving high selectivity and efficiency in an H-type cell remains challenging due to the complexity of the GOR mechanisms, intermediate conditions of 50 mM and 1.5 V at temperatures below 50°C are proposed to maximize FA production while minimizing competition with the formation of other products. Finally, DFT results confirmed that the presence of Sn/SnO_2 promotes the Ni activity thus enhancing the adsorption of glucose and boosting the oxohydroxyde formation.

Acknowledgement

This work was financially supported by the SyDECat project from the Spanish MCIN/AEI/FEDER (PID2022-136883OB-C22). The authors acknowledge funding from project PID2020-116612RB-C32, PID2022-138491OB-C33, Generalitat de Catalunya 2021SGR01581 and 2021SGR00457 European Union NextGenerationEU/PRTR. J.L. is a Serra Húnter Fellow and is grateful to the ICREA Academia program and projects MICINN/FEDER PID2021-124572OB-C31 and GC 2021 SGR 01061. This study is part of the Advanced Materials program and In-CAEM project, supported by MCIN with funding from the European Union Next Generation EU (PRTR-C17.I1) and by Generalitat de Catalunya. This work is in the framework of the Universitat Autònoma de Barcelona Materials Science PhD program. The authors acknowledge the use of instrumentation as well as the technical advice provided by the Joint Electron Microscopy Center at ALBA (JEMCA). ICN2 acknowledges funding from Grant IU16-014206 (METCAM-FIB) funded by the European Union through the European Regional Development Fund (ERDF), with the support of the Ministry of Research and Universities, Generalitat de Catalunya. ICN2 is a founding member of e-DREAM.[40] IREC and ICN2 are both funded by the CERCA Program/Generalitat de Catalunya. ICN2 thank the support from project NANOGEN (PID2020-116093RB-C43), funded by MCIN/ AEI/10.13039/501100011033/ and by "ERDF A way of making Europe", by the "European Union". ICN2 acknowledge the support from the Severo Ochoa Programme (MINECO, grant no. CEX2021-001214-S).

Conflict of Interest

The authors declare not conflict of interest

Keywords

Electrochemistry, formic acid, glucose oxidation reaction, nickel, NiSn.

References

[1] W. J. Liu, Z. Xu, D. Zhao, X. Q. Pan, H. C. Li, X. Hu, Z. Y. Fan, W. K. Wang, G. H. Zhao, S. Jin, G. W. Huber, H. Q. Yu, *Nat. Commun.* **2020**, *11*, 1–11.

[2] Y. Q. Zhu, H. Zhou, J. Dong, S. M. Xu, M. Xu, L. Zheng, Q. Xu, L. Ma, Z. Li, M. Shao, H. Duan, *Angew. Chemie - Int. Ed.* **2023**, *62*, DOI 10.1002/anie.202219048.

[3] H. Zhou, Y. Ren, B. Yao, Z. Li, M. Xu, L. Ma, X. Kong, L. Zheng, M. Shao, H. Duan, *Nat. Commun.* **2023**, *14*, 1–12.

[4] Y. Wang, M. Xu, X. Wang, R. Ge, Y. Q. Zhu, A. Z. Li, H. Zhou, F. Chen, L. Zheng, H. Duan, *Sci. Bull.* **2023**, *68*, 2982–2992.

[5] L. Ostervold, S. I. Perez Bakovic, J. Hestekin, L. F. Greenlee, *RSC Adv.* **2021**, *11*, 31208–31218.

[6] A. Anil, J. White, E. Campos dos Santos, I. Terekhina, M. Johnsson, L. G. M. Pettersson, A. Cornell, G. Salazar-Alvarez, *J. Mater. Chem. A* **2023**, *11*, 16570–16577.

[7] X. Su, Z. Pan, L. An, *Int. J. Energy Res.* **2019**, *43*, 7433–7443.

[8] A. M. Bartrom, J. Ta, T. Q. Nguyen, J. Her, A. Donovan, J. L. Haan, *J. Power Sources* **2013**, *229*, 234–238.

[9] L. Q. Wang, M. Bellini, J. Filippi, M. Folliero, A. Lavacchi, M. Innocenti, A. Marchionni, H. A. Miller, F. Vizza, *Appl. Energy* **2016**, *175*, 479–487.

[10] M. Fleischmann, K. Korinek, D. Pletcher, *J. Electroanal. Chem.* **1971**, *31*, 39–49.

[11] Z. Liu, Y. Shen, *ACS Appl. Energy Mater.* **2022**, *5*, 11723–11731.

[12] A. M. Abdelrahim, M. G. Abd El-Moghny, M. E. El-Shakre, M. S. El-Deab, *RSC Adv.* **2023**, *13*, 1811–1822.

[13] V. P. Ananikov, *ACS Catal.* **2015**, *5*, 1964–1971.

[14] P. Sabatier, *Catalysis in Organic Chemistry*, **1922**.

[15] S. Jiao, N. Kang, M. Liu, Y. Zhang, Y. Li, B. Maryam, P. Zhang, X. Liu, *Catalysts* **2016**, *14*, 1–23.

[16] C. Lin, P. Zhang, S. Wang, Q. Zhou, B. Na, H. Li, J. Tian, Y. Zhang, C. Deng, L. Meng, J. Wu, C. Liu, J. Hu, L. Zhang, *J. Alloys Compd.* **2020**, *823*, 153784.

[17] X. Lin, H. Zhong, W. Hu, J. Du, *Inorg. Chem.* **2023**, *62*, 10513–10521.

[18] N. Wei, S. Zhang, X. Yao, Y. Feng, V. Nica, J. Yang, Q. Zhou, *Sep. Purif. Technol.* **2024**, *343*, 127178.

[19] D. Chai, W. Wang, F. Wang, Y. Kang, Y. Yang, Z. Lei, *Electrochim. Acta* **2016**, *189*, 295–302.

[20] DandanTu, B. Wu, B. Wang, C. Deng, Y. Gao, *Appl. Catal. B Environ.* **2011**, *103*, 163–168.

[21] R. M. Abdel Hameed, A. E. Fahim, N. K. Allam, *J. Mol. Liq.* **2020**, *297*, 111816.

[22] X. Yu, J. Liu, J. Li, Z. Luo, Y. Zuo, C. Xing, J. Llorca, D. Nasiou, J. Arbiol, K. Pan, T. Kleinhanns, Y. Xie, A. Cabot, *Nano Energy* **2020**, *77*, DOI 10.1016/j.nanoen.2020.105116.

[23] Z. Luo, J. Lu, C. Flox, R. Nafria, A. Genç, J. Arbiol, J. Llorca, M. Ibáñez, J. R. Morante, A. Cabot, *J. Mater. Chem. A* **2016**, *4*, 16706–16713.

[24] W. Du, K. E. MacKenzie, D. F. Milano, N. A. Deskins, D. Su, X. Teng, *ACS Catal.* **2012**, *2*, 287–297.

[25] D. W. Boukhvalov, G. D'Olimpio, J. Liu, C. Ghica, M. C. Istrate, C. N. Kuo, G. G. Politano, C. S. Lue, P. Torelli, L. Zhang, A. Politano, *Chem. Commun.* **2023**, 6040–6043.

[26] X. Tang, B. Zhang, Y. Li, Y. Xu, Q. Xin, W. Shen, *J. Mol. Catal. A Chem.* **2005**, *235*, 122–129.

[27] T. H. Huang, H. S. Zheng, Y. M. Cheng, C. W. Liu, S. W. Lee, J. H. Wang, K. W. Wang, *Sustain. Energy Fuels* **2019**, *3*, 3352–3362.

[28] C. W. Liu, Y. W. Chang, Y. C. Wei, K. W. Wang, *Electrochim. Acta* **2011**, *56*, 2574–2581.

[29] N. A. M. Barakat, F. S. Al-Mubaddel, M. Rezual Karim, M. Alrashed, H. Yong Kim, *Int. J. Hydrogen Energy* **2018**, *43*, 21333–21344.

[30] J. Li, Z. Luo, Y. Zuo, J. Liu, T. Zhang, P. Tang, J. Arbiol, J. Llorca, A. Cabot, *Appl. Catal. B Environ.* **2018**, *234*, 10–18.

[31] J. Li, X. Xu, X. Yu, X. Han, T. Zhang, Y. Zuo, C. Zhang, D. Yang, X. Wang, Z. Luo, J. Arbiol, J. Llorca, J. Liu, A. Cabot, *ACS Appl. Mater. Interfaces* **2020**, *12*, 4414–4422.

[32] C. C. L. McCrory, S. Jung, J. C. Peters, T. F. Jaramillo, *J. Am. Chem. Soc.* **2013**, *135*, 16977–16987.

[33] G. Kresse and J. Furthüller, *Phys Rev B Condens Matter* **1996**, *54*, 11169–11186.

[34] G. Kresse, J. Hafner, *Phys. Rev. B* **1994**, *49*, 14251–14269.

[35] J. P. Perdew, K. Burke, M. Ernzerhof, *Phys. Rev. Lett.* **1996**, *77*, 3865–3868.

[36] P. E. Blöchl, *Phys. Rev. B* **1994**, *50*, 17953–17979.

[37] H. J. M. and J. D. Pack, *Phys. Rev. B* **1976**, *13*, 5188–5192.

[38] J. Li, C. Xing, Y. Zhang, T. Zhang, M. C. Spadaro, Q. Wu, Y. Yi, S. He, J. Llorca, J. Arbiol, A. Cabot, C. Cui, *Small* **2021**, *17*, DOI 10.1002/smll.202006623.

[39] L. Xiao, J. T. Lu, P. F. Liu, L. Zhuang, J. W. Yan, R. G. Hu, H. W. Mao, C. J. Lin, *Chinese Chem. Lett.* **2005**, *16*, 419–422.

[40] R. Ciancio, R. E. Dunin-Borkowski, E. Snoeck, M. Kociak, R. Holmestad, J. Verbeeck, A. I. Kirkland, G. Kothleitner, J. Arbiol, *Microsc. Microanal.* **2022**, *28*, 2900–2902.